RSC Advances

PAPER

View Article Online
View Journal | View Issue

Cite this: *RSC Adv.*, 2024, **14**, 7061

Energy transfer for $Ce^{3+} \rightarrow Tb^{3+} \rightarrow Sm^{3+}$ induced bright white emission in single-phase $CaLa_4(SiO_4)_3O:Ce^{3+}$, Tb^{3+}, Sm^{3+} phosphors and their application in white-light-emitting diodes

Bo Yuan, *[a] Jiaxuan Gou,[a] Chaochao Qi,[a] Li Kong,[a] Mingyang Qu,[a] Guoyan Luan[a] and Xiangting Zhang[b]

Received 17th January 2024
Accepted 13th February 2024

DOI: 10.1039/d4ra00443d

rsc.li/rsc-advances

The emergence of phosphor-converted white-light-emitting diodes has crucial significance in the sustainable development of energy; hence, the evolution of phosphors with eminent luminescence and high stability is imperative. In this study, a tri-doped system composed of rare earth ions Ce^{3+}, Tb^{3+}, and Sm^{3+} incorporated into a $CaLa_4(SiO_4)_3O$ host is reported, and the energy transfer, tunable single-phase white emission, and favorable thermostability of the Ce^{3+}–Tb^{3+}–Sm^{3+} system were explored. Rietveld refinement results coincided with the original model of the crystal structure, and a band gap energy of 4.612 eV calculated using density functional theory (DFT) demonstrated the system as an appropriate luminescent host with a wide energy gap. Furthermore, ET processes for $Ce^{3+} \rightarrow Tb^{3+}$, $Tb^{3+} \rightarrow Sm^{3+}$, and $Ce^{3+} \rightarrow Tb^{3+} \rightarrow Sm^{3+}$ were investigated *via* steady-state photoluminescence and decay measurements. Besides, the activation energies of CLSO:3%Ce^{3+}, 9%Tb^{3+}, *y*%Sm^{3+} ($y = 7$, 9) were 0.205 eV and 0.223 eV, respectively, showing outstanding thermal quenching resistance. Devices made with LED beads containing CLSO:3%Ce^{3+}, 9%Tb^{3+}, *y*%Sm^{3+} ($y = 7$, 9) phosphors exhibited bright white light with CCT ≈ 3586 and 3307 K and Ra ≈ 81.0 and 78.5, respectively. This study demonstrates that energy transfer for Ce^{3+}–Tb^{3+}–Sm^{3+} in a tri-doped system offers an interesting design prospect for promoting single-phase white emission phosphors.

1. Introduction

Lanthanide activated inorganic luminescent materials with superior features for color modulation covering almost the entire range of visible light have been found to possess important application value in the lighting field.[1–3] While energy-conserving phosphor-converted white-light-emitting diodes (pc-WLEDs) are predicted to become the fourth generation artificial lighting,[4,5] currently, the commercial combined patterns of white LEDs involve a InGaN blue chip + YAG:Ce^{3+} yellow phosphor. However, the imperfections of its color rendering and color temperature are still criticized.[6,7] There are two ways for overcoming this problem: one is the supplementation of red components that can effectively absorb blue emission; the other is to apply a mixture of blue, green and yellow phosphor coating with an ultraviolet chip to acquire a soft white light. However, both the schemes involve reabsorption and aging rate differences for mixed phosphors, which can affect luminescence efficiency.[8–11] Current effective alternate solutions to eliminate these inadequacies are expected to involve a single-phase white emission phosphor with high thermal stability, and one that would also be more appropriate for the ultraviolet region.[12]

Based on the current situation, following tactics are applied to induce white emission for rare earth ion-doped single-phase phosphors: (I) activation of a single ion in a low phonon energy host. Although white light may be derived from Dy^{3+} ions for f–f transition or by Eu^{2+} ion emission from d–f transition, the low emission efficiency of f–f transition due to cross relaxation and inadequate red emission for d–f transition remain disputed.[13–15] (II) Varying the ratio of emission centers and with an excitation of a particular wavelength when multiple activated ions are mixed into a feasible matrix. However, the degradation of white light due to a slight deviation in the excitation wavelength is a major challenge.[16,17] (III) Energy transfer among different dopants. However, the current energy-transfer system mostly involves double doping, and the energy-transfer efficiency and luminescent color need to be further improved.[18,19] Thus, more research needs to be carried out on energy transfer in tri-doped systems.

The energy transfer in tri-doped systems offers better patterns that can make up for the above deficiencies and realize

[a]*College of Petrochemical Engineering, Jilin Institute of Chemical Technology, Jilin 132000, P. R. China. E-mail: yb19880613@163.com; Tel: +86 432 62185157*
[b]*College of Chemistry and Chemical Engineering, Henan Normal University, Xinxiang 453007, P. R. China*

high-quality white light in a single component, but the implementation conditions are more stringent. As is well known, Ce^{3+} ions can have an outstanding effect as vital sensitizers due to their 4f electronic configuration; while Tb^{3+} and Sm^{3+} ions are also effective doping activations for green and red emission, respectively.[20–22] Hence, the effective energy absorbed by Ce^{3+} eventually transferring to Sm^{3+} through Tb^{3+} in the Ce^{3+}–Tb^{3+}–$(Sm^{3+})_n$ model can be considered to produce white light emission. Furthermore, the crystal field environment in which the above three ions reside is also crucial to this process. Silicate is universally recognized for its simple synthesis, remarkable thermal stability and low cost, and has been substantiated as an admirable luminescent substrate.[23] $A_2B_8(SiO_4)_6O_2$ (A = alkaline metal, B = rare earth), as oxyapatite-related silicate constituents, are favorable rare earth-activating matrixes in the silicate family. These compounds possess two special sites in their lattice structures: a seven-coordinated 6h site with the C_s point symmetry and a nine-coordinated 4f site with the C_3 point symmetry, which provide lattice placeholders for different categories of emission of the activation ions.[24] In this research, it is demonstrated that the $CaLa_4(SiO_4)_3O$ (henceforth shortened as CLSO) oxyapatite silicate host exhibited energy transfer for the Ce^{3+}–Tb^{3+}–Sm^{3+} tri-doped systems for white-light emission. The ET principles of Ce^{3+}–Tb^{3+}, Tb^{3+}–Sm^{3+}, and Ce^{3+}–Tb^{3+}–Sm^{3+} ions were investigated in detail on the strength of the steady-state photoluminescence process and lifetime consequences. Impressively, the results indicated that the chromaticity coordinates of CLSO:Ce^{3+}, Tb^{3+}, Sm^{3+} phosphors can enter the white zone by alteration of the Sm^{3+} ion concentration, and the performance of the thermal stabilities in the phosphors was ideal. Finally, the application test for a device assembly based on UV LED chips was carried out. This is the first study that has reported achieving white-light emission through the Ce^{3+}–Tb^{3+}–Sm^{3+} triply-doped CLSO system.

2. Experimental

2.1 Material fabrication

A solid-phase synthesis was applied to the preparation of a series of CLSO:Ce^{3+}/Tb^{3+}/Sm^{3+} phosphors. The primary materials mainly consisted of $CaCO_3$, SiO_2, La_2O_3, CeO_2, Tb_4O_7 and Sm_2O_3 (analytical reagent grade), and all were obtained from Sinopharm Chemical Reagent. The above compounds were combined in an agate mortar according to the proportion of the chemical constituents. After mixing thoroughly, the mixed samples were transferred to a muffle furnace for presintering at 1000 °C for 1 h, and soon afterwards programmed to 1500 °C in a tube furnace and maintained at that temperature for 4 h under a reduction atmosphere of N_2 (95%)/H_2 (5%). Finally, after natural cooling, the mixtures were crushed to obtain powder products for the following tests.

2.2 White LED prototype fabrication

Serial white LED devices were fabricated with a coating on the cover of commercial 360 nm LED chips with the as-synthesized CLSO:3%Ce^{3+}, 9%Tb^{3+}, y%Sm^{3+} (y = 7, 9) phosphors. The working voltage of 3.0 V and bias current of 20 mA were employed to operate the fabricated LED prototypes.

2.3 Measurements and characterization

The characterization tests for obtaining the phase data and crystal structure were based on X-ray diffraction (XRD) patterns obtained using a Bruker AXS D8 diffractometer, in the 2θ range of 10° to 80°, with CuKα radiation. The crystal structure refinement was resolved employing the Rietveld method in the GSAS program. Evaluation of the band structures for CLSO was performed based on density functional theory calculations performed in the CASTAP module. The steady-state spectra for the excitation and emission were measured on an Edinburgh FS5 spectrometer with a 150 W xenon lamp. The decay curves of the transient-state luminescence measurements were recorded by nanosecond and millisecond pulse lasers as the excitation sources on the Edinburgh FLS980 spectrometer. The luminescence thermal stability was investigated on the same system equipped with a temperature controller. The electroluminescence and correlative performances (CIE, CRI and CCT) of the LED prototypes were traced utilizing an EVERFINE HAAS-2000 LED Spectro-photocolorimeter system.

3. Results and discussion

3.1 Crystal structure and simple phase analysis

The XRD patterns of the samples with different doping content are presented in Fig. 1a. All the results could be well indexed to the crystal structure of CLSO derived from the standard diffraction data (JCPDS 71-1368), suggesting that the signals of other components were not observed in these samples. This further illustrates that the crystal structure of CLSO could be retained even with the small introduction of rare earth ions, and that the Ce^{3+}, Tb^{3+} and Sm^{3+} ions had been dissolved into the crystal lattice of the host. It is suggested that Ce^{3+} (r = 1.07 Å for CN = 7 and r = 1.19 Å for CN = 9), Tb^{3+} (r = 0.98 Å for CN = 7 and r = 1.09 Å for CN = 9) and Sm^{3+} (r = 1.02 Å for CN = 7 and r = 1.13 Å for CN = 9) occupy the La^{3+} (r = 1.10 Å for CN = 7 and r = 1.22 Å for CN = 9) lattice in CLSO:Ce^{3+}, Tb^{3+}, Sm^{3+} considering the ionic radii, valence state, and atomic coordination.[24–26] The model of the space unit for CLSO was constituted employing Diamond software and based on the literature. As exhibited in Fig. 1b, the CLSO compound crystallized in the hexagonal oxyapatite structure with the space group $P6_3/m$ (176), with the lattice parameters $a = b$ = 9.651 Å, c = 7.151 Å, V = 576.8 Å. In this structure, Ca1/La1 ions are situated at the 4f site with a nine-fold coordination and Ca2/La2 ions are situated at the 6h site with a seven-fold coordination, which are linked to the isolated SiO_4 tetrahedron.[27–29] The obvious crystal field environment difference between the 6h and 4f sites will lead to diverse crystal field strengths and a nephelauxetic effect for the emission centers in the host.[30]

Rietveld refinement of the XRD patterns for the CLSO and CLSO:Ce^{3+} samples was performed (the recorded, computed and difference XRD profiles are depicted in Fig. 2). The refined fraction factors were R_p = 11.85%, R_{wp} = 13.25%, and χ^2 = 3.881

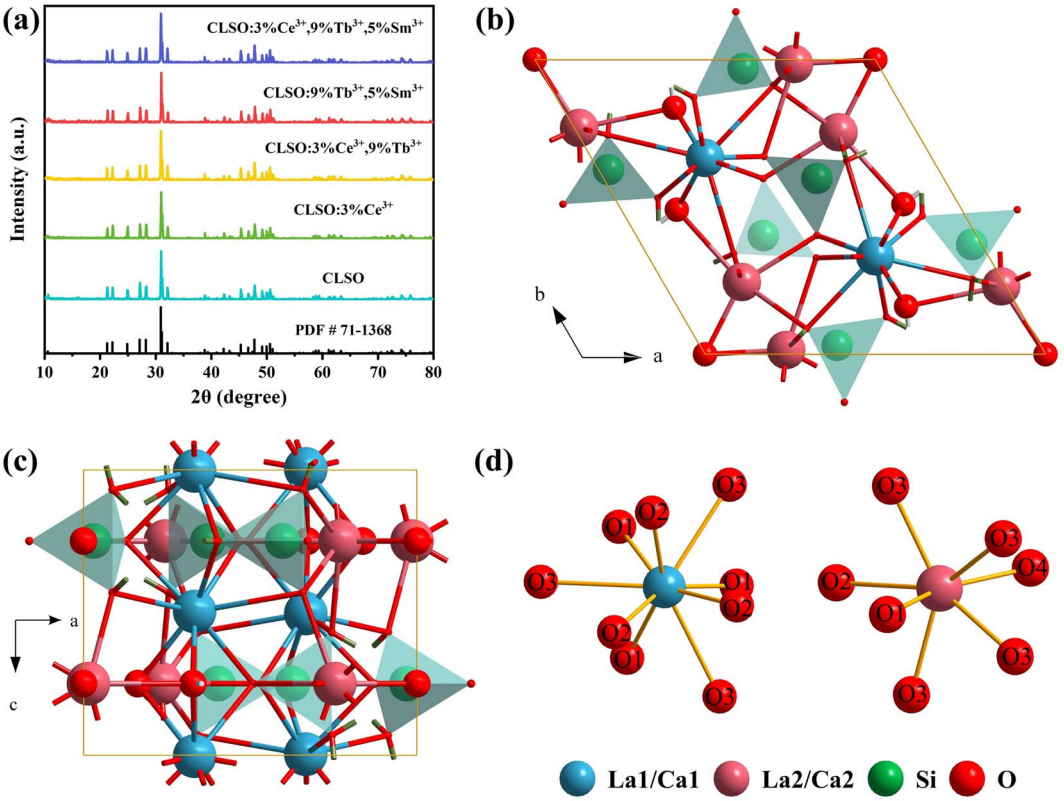

Fig. 1 (a) XRD patterns for the prepared CLSO samples, CLSO:Ce^{3+}/Tb^{3+}/Sm^{3+} phosphors and the CLSO standard data (PDF # 71-1368). (b and c) Crystal structure of the CLSO host. (d) Coordination environments for cation sites (La1/Ca1 and La2/Ca2).

for CLSO and $R_p = 10.94\%$, $R_{wp} = 12.11\%$, and $\chi^2 = 3.395$ for CLSO:Ce^{3+}, indicating that the refinements of the crystal structures were dependable. The cell constants of CLSO and CLSO:Ce^{3+} were $a = b = 9.651$ Å, $c = 7.155$ Å, $V = 577.15$ Å^3 and $a = b = 9.650$ Å, $c = 7.146$ Å, $V = 576.53$ Å^3, respectively, with the final particular refinement information summarized in Tables 1 and 2.

Furthermore, on the basis of the refinement, calculations of the electronic band structure for CLSO were performed utilizing Materials Studio software in the CASTAP module, as exhibited in Fig. 3a, to investigate the promotion effect of the electron band environment on the luminescence. The top of the valence band and bottom of the conduction band were both situated at the G point in the Brillouin region, indicating that CLSO had a direct band gap.[31] The computed result of E_g (4.612 eV) showed it belonged to an insulator material with a wide band gap.[32,33] It is predicted that CLSO would be a good luminescent host possessing a sufficient energy gap to contain the energy levels of the luminescent ions, which would be favorable for energy absorption and utilization of the 4f–5d transition for rare

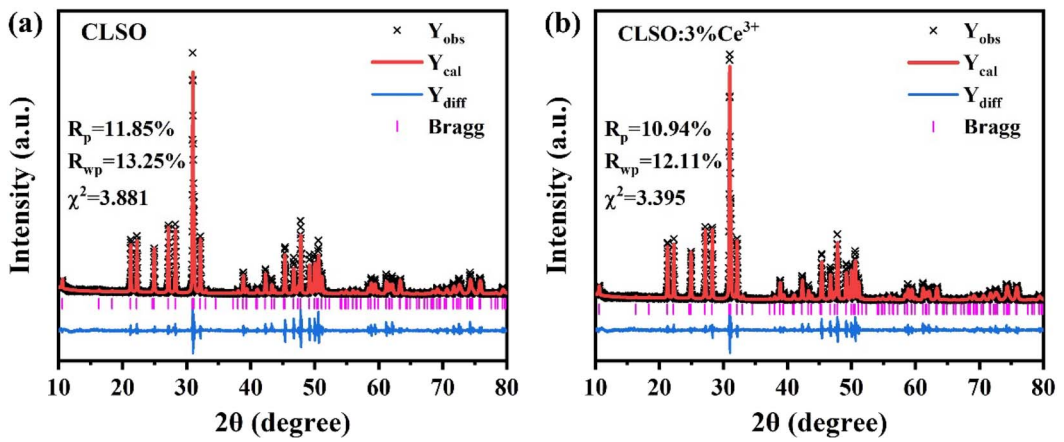

Fig. 2 Rietveld refinements of the XRD patterns for (a) CLSO and (b) CLSO:3%Ce^{3+} samples.

Table 1 Crystal structural data and atomic coordinates of CLSO as a result of Rietveld refinement

		Atomic coordinates and site occupancy fraction				
Crystallographic data of CLSO		Atom	x	y	z	SOF
Space group	$P6_3/m$	La1	0.3333	0.6666	0.0031 (1)	0.522 (1)
a/Å	9.6510 (1)	Ca1	0.3333	0.6666	0.0031 (1)	0.478
b/Å	9.6510 (1)	La2	0.2460 (1)	0.0142 (1)	0.2500	0.983 (1)
c/Å	7.1550 (1)	Ca2	0.2460 (1)	0.0142 (1)	0.2500	0.017
α/deg	90	Si1	0.3758 (1)	0.3976 (1)	0.2500	1
β/deg	90	O1	0.4696 (4)	0.5961 (4)	0.2500	1
γ/deg	120	O2	0.4933 (4)	0.3261 (4)	0.2500	1
V/Å^3	577.1450 (3)	O3	0.2561 (3)	0.3419 (5)	0.0693 (4)	1
R_p/%	11.85	O4	0.0000	0.0000	0.2500	1
R_{wp}/%	13.25					
χ^2	3.881					

Table 2 Crystal structural data and atomic coordinates of CLSO:3%Ce^{3+} as a result of Rietveld refinement

		Atomic coordinates and site occupancy fraction				
Crystallographic data of CLSO:3% Ce^{3+}		Atom	x	y	z	SOF
Space group	$P6_3/m$	La1	0.3333	0.6666	0.0038 (1)	0.4902 (1)
a/Å	9.6505 (1)	Ca1	0.3333	0.6666	0.0038 (1)	0.4757
b/Å	9.6505 (1)	La2	0.2449 (1)	0.0151 (1)	0.2500	0.9532 (1)
c/Å	7.1460 (1)	Ca2	0.2449 (1)	0.0151 (1)	0.2500	0.0142
α/deg	90	Si1	0.3785 (1)	0.4069 (1)	0.2500	1
β/deg	90	O1	0.4697 (4)	0.5958 (4)	0.2500	1
γ/deg	120	O2	0.4954 (4)	0.3242 (4)	0.2500	1
V/Å^3	576.5260 (3)	O3	0.2594 (3)	0.3464 (5)	0.0692 (4)	1
R_p/%	10.94	O4	0.0000	0.0000	0.2500	1
R_{wp}/%	12.11	Ce1	0.3333	0.6666	0.0038 (1)	0.0341
χ^2	3.395	Ce2	0.2449 (1)	0.0151 (1)	0.2500	0.0326

earth ions with a broad band emission.[34,35] The distributions of the total and partial density of states for the calculated electronic band structure in CLSO are shown in Fig. 3b. It could be further understood that the conduction band constituted the electronic orbital in the CaLa-4s 3d and Si-4s 3p states while the valence band involved the O-2s 2p electronic states.

The experimental value of the band gap can be related to the diffuse reflectance spectra (Fig. 3c), and can be estimated through the equation:[36]

$$(\alpha h\nu)^n = A(h\nu - E_g) \quad (1)$$

where α is the absorption coefficient, $h\nu$ represents the photon energy, and A is a proportional constant and the direct band gap for $n = 2$. The value of α is associated with the coefficient of reflection R:[37]

$$\alpha = \frac{(1 - R^2)}{2R} \quad (2)$$

The energy band value was determined to be 4.6 eV for the CLSO sample as shown in the inset (the diffuse reflectance spectra treated by the Kubelka–Munk function). The theoretical

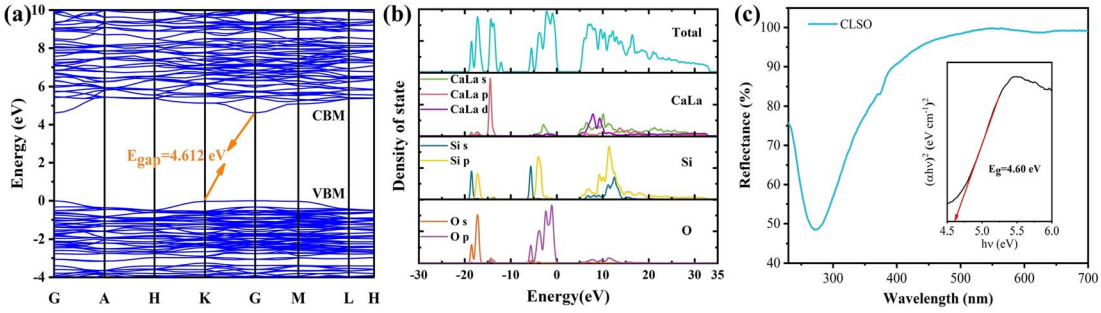

Fig. 3 (a) Band gap structure and energy value of the CLSO host. (b) Total and partial density of states (DOS) for CLSO by DFT calculations. (c) Diffuse reflectance spectra of CLSO; inset reveals the calculated E_g value obtained with the Kubelka–Munk function.

value based on DFT (4.612 eV) was almost equal to the experimental one, highlighting the consistency of the two results.

3.2 Luminescence properties of CLSO:Ce^{3+}, CLSO:Tb^{3+} and CLSO:Sm^{3+}

Fig. 4 presents the photoluminescence excitation and emission spectra of Ce^{3+}/Tb^{3+}/Sm^{3+} single-doped CLSO. At 390 nm emission wavelength, the excitation spectrum derived from the parity-allowed 4f–5d transitions of Ce^{3+} ion showed a broad band from 250 to 400 nm (Fig. 4a). Under 287 nm excitation, the Ce^{3+}-doped CLSO demonstrated an intense emission spectrum involving an asymmetric emission band with a maximum at 390 nm, related to the transition from the excited state 5d to the doublet levels $^2F_{7/2}$ and $^2F_{5/2}$ of 4f. As displayed in Fig. 4b, the emission spectrum of Tb^{3+} was constituted by a cluster of strong lines at 491, 542, 583 and 624 nm on account of the characteristic emission for $^5D_4 \rightarrow {}^7F_J$ (J = 6, 5, 4, and 3) excited at 377 nm, of which the green emission of 542 nm had the greatest intensity. Monitoring the dominant green emission, a PLE spectrum with a remarkable absorption line at 377 nm (the $^7F_6 \rightarrow {}^5D_3$ transition) was obtained. In Fig. 4c, when monitored at 598 nm, the excitation spectrum of CLSO:Sm^{3+} appeared in the spectral range of 200–500 nm and included a sequence of narrow lines at 345 nm ($^6H_{5/2}$–$^4H_{7/2}$), 361 nm ($^6H_{5/2}$–$^4F_{9/2}$), 372 nm ($^6H_{5/2}$–$^4D_{5/2}$), 402 nm ($^6H_{5/2}$–$^4K_{11/2}$), 415 nm ($^6H_{5/2}$–$^6P_{5/2}$) and 474 nm ($^6H_{5/2}$–$^4I_{11/2}$), respectively. Upon the characteristic excitation, several emission bands at 564, 598 and 648 nm emerged in the PL spectrum, assigned to the transition of Sm^{3+} ion for $^4G_{5/2} \rightarrow {}^6H_{5/2}$, $^4G_{5/2} \rightarrow {}^6H_{7/2}$ and $^4G_{5/2} \rightarrow {}^6H_{9/2}$, respectively.

3.3 Luminescence properties and energy transfer of CLSO:Ce^{3+}, Tb^{3+}

The energy-transfer system involving double doping is a precondition for tri-doped systems, and correspondingly, the energy transfer from Ce^{3+} to Tb^{3+} is the primary area of concern here. To research the process in the CLSO host, the emission spectra with invariant Ce^{3+} concentration (3%) while altering the Tb^{3+} content were monitored, as shown in Fig. 5a; meanwhile Fig. 5b demonstrates the curve graphs of the variation in the emission intensity based on the Tb^{3+} contents. With the gradual augment of the Tb^{3+} content, the green emission strength derived from Tb^{3+} transition increased along with the decrease in the Ce^{3+} violet emission at 347 nm excitation. The enhanced green emission of 542 nm (Tb^{3+}) by degree is the credit for the energy transfer of $Ce^{3+} \rightarrow Tb^{3+}$. The chromaticity coordinates for CLSO:3%Ce^{3+}, y%Tb^{3+} as shown in Fig. 5c, were regulated from (0.276, 0.223) to (0.338, 0.567), displaying a color fluctuation from violet to green for y (1–13). All the relevant coordinate results are aggregated and listed in Table 3.

The fluorescence lifetime of Ce^{3+} ions can be a direct response to the luminescence kinetics and energy transfer;

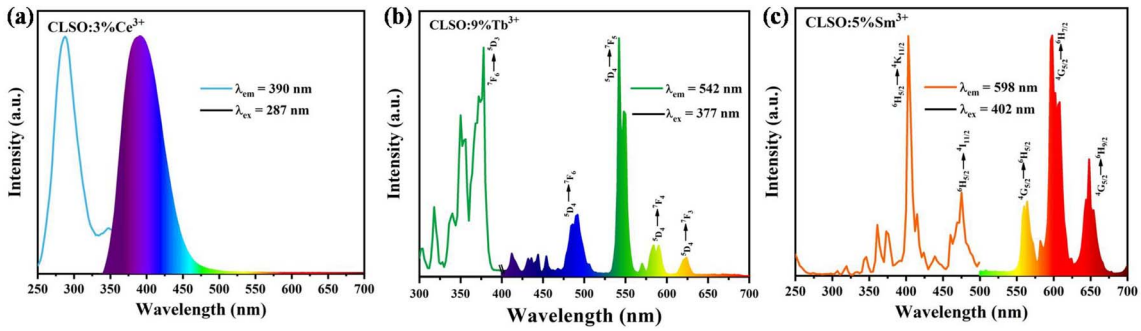

Fig. 4 (a) Excitation and emission spectra of the CLSO:3%Ce^{3+} phosphor. (b) Excitation and emission spectra of the CLSO:9%Tb^{3+} phosphor. (c) Excitation and emission spectra of the CLSO:5%Sm^{3+} phosphor.

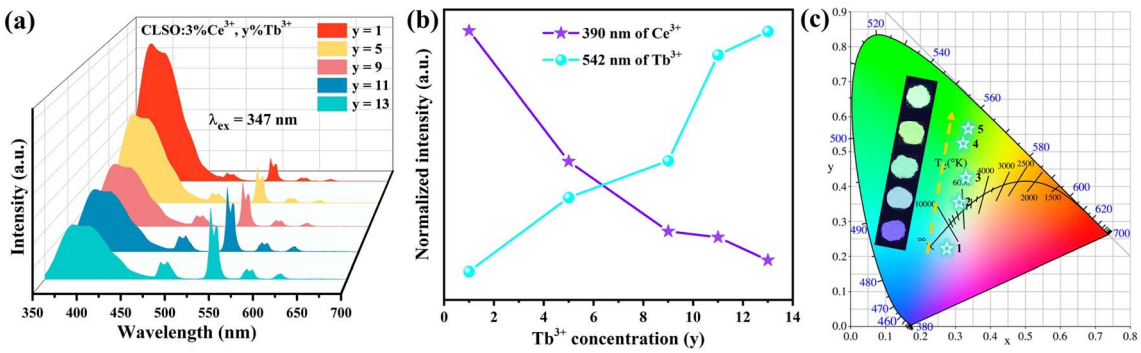

Fig. 5 (a) Emission spectra of CLSO:3%Ce^{3+}, y%Tb^{3+} (y = 1–13). (b) Variation in the emission intensity *versus* the Tb^{3+} content. (c) CIE chromaticity coordinates for these phosphors.

Table 3 CIE chromaticity coordinates for CLSO:3%Ce^{3+}, y%Tb^{3+} phosphors

Sample no.	Sample	CIE coordinates (x, y)
1	CLSO:3%Ce^{3+}, 1%Tb^{3+}	(0.276, 0.223)
2	CLSO:3%Ce^{3+}, 5%Tb^{3+}	(0.312, 0.355)
3	CLSO:3%Ce^{3+}, 9%Tb^{3+}	(0.331, 0.425)
4	CLSO:3%Ce^{3+}, 11%Tb^{3+}	(0.323, 0.524)
5	CLSO:3%Ce^{3+}, 13%Tb^{3+}	(0.338, 0.567)

therefore, the decay curves of the CLSO:3%Ce^{3+}, y%Tb^{3+} (0–13) samples were explored as indicated in Fig. 6. The lifetime curve for the singly Ce^{3+}-doped CLSO could be well fitted into a single-exponential function while that of the other co-doped samples could be well-explained by a double-exponential equation:

$$I = I_0 \exp(-t/\tau) \quad (3)$$

$$I = I_0 + A_1 \exp(-t/\tau_1) + A_2 \exp(-t/\tau_2) \quad (4)$$

where I_0 and I express the luminescence intensities at time 0 and t, respectively, and τ_1 and τ_2 are the decay times for the exponential components, respectively. It can be found that as more Tb^{3+} ions are brought in, the attenuation degree for the lifetime curves of Ce^{3+} ion also increased by degrees. The different effective fluorescence lifetimes can be defined as:[38]

$$\tau = \frac{\int_0^\infty tI(t)\mathrm{d}t}{\int_0^\infty I(t)\mathrm{d}t} \quad (5)$$

where $I(t)$ expresses the intensity at time t. The decay times of Ce^{3+} ion were determined to be 25.71, 24.94, 23.93, 23.02, 22.92 and 21.73 ns, respectively, for the values of $y = 0$, 1, 5, 9, 11, 13 for the Tb^{3+} contents, whereby the tendency toward shorter lifetimes substantiated the energy-transfer process.

The energy-transfer efficiency (η_T) from the sensitizer (Ce^{3+}) to activator (Tb^{3+}) could be resolved based on the corresponding formula by Paulose *et al.*:[39]

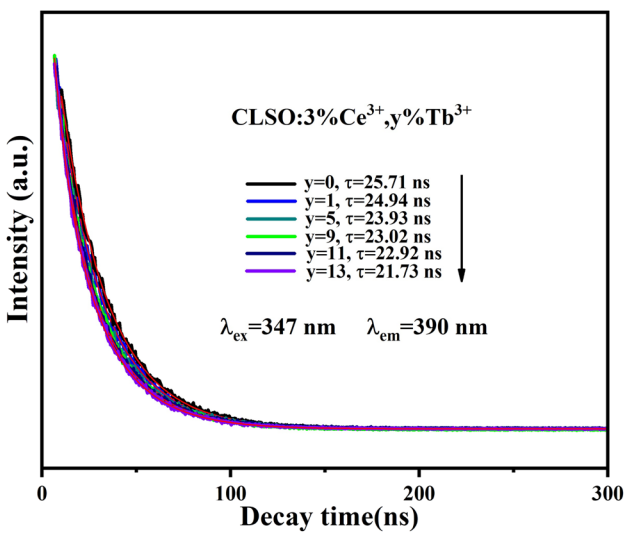

Fig. 6 Decay curves for Ce^{3+} emission from CLSO:3%Ce^{3+}, y%Tb^{3+} (y = 0–13) (excited at 347 nm, monitored at 390 nm).

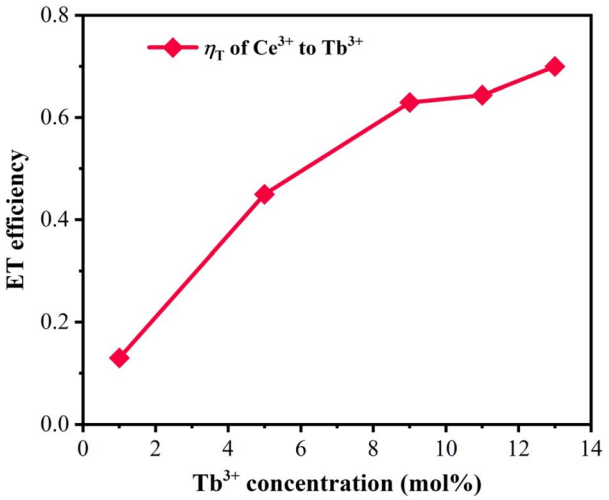

Fig. 7 Dependence of energy-transfer efficiency η_T on Tb^{3+} concentration.

$$\eta_T = 1 - \frac{I_S}{I_{SO}} \quad (6)$$

where I_{SO} and I_S denote the luminous intensities of Ce^{3+} in CLSO:3%Ce^{3+} and CLSO:3%Ce^{3+}, y%Tb^{3+} (0–13), respectively. It could be inferred from Fig. 7 that η_T showed a trend of gradually rising with the increase in the introduced amount of Tb^{3+} ions, ultimately approaching saturation. The maximum value of 70% for η_T at $y = 0.13$ revealed the efficient energy-transfer process.

3.4 Energy transfer for $Tb^{3+} \rightarrow Sm^{3+}$ in the CLSO host

The PL spectra with the constant Tb^{3+} amount and varied content of Sm^{3+} in the CLSO host at 377 nm excitation are depicted in Fig. 8a, while Fig. 8b demonstrates the curve graphs of the variation in emission intensity with the variation in Sm^{3+} content. In spite of the Tb^{3+} content remaining the same (9%), the green special emission (Tb^{3+}) was reduced with the increase in Sm^{3+} concentration, while simultaneously, that of Sm^{3+} was promoted until a maximum value at $y = 5$, and then decreased. The color modulation of the CLSO:9%Tb^{3+}, y%Sm^{3+} (y = 1–13) phosphor could also be demonstrated through the energy-transfer process, and the CIE graph is shown in Fig. 8c. The chromatic coordinates could be converted from green emission (0.403, 0.476) to yellow (0.393, 0.387) approaching white light in the wake of the Sm^{3+} content advancing in value of y from 1 to 13, as shown in Table 4. The fundamental findings suggest that white light emission could be anticipated for the Ce^{3+}, Tb^{3+}, Sm^{3+} tri-doped system.

The lifetime curves of Tb^{3+} ions monitored at the emission wavelength of 542 nm with varying the content of Sm^{3+} ions were evaluated to explore the energy transfer from Tb^{3+} to Sm^{3+} in CLSO. As demonstrated in Fig. 9, the decay curve for singly Tb^{3+}-doped CLSO could be well fitted into a single-exponential function, eqn (3), while that of the other co-doped samples could be well-explained by a double-exponential equation, eqn (4). The effective lifetimes were determined to be 2.102, 2.029, 2.014, 1.905, 1.814, 1.728 and 1.701 ms, respectively, by means

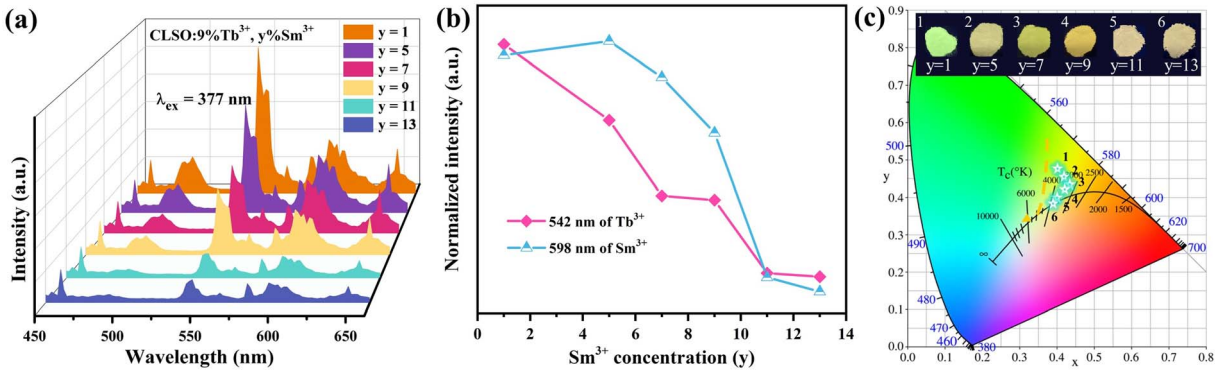

Fig. 8 (a) Emission spectra of CLSO:9%Tb^{3+}, *y*%Sm^{3+} (*y* = 1–13). (b) Variation in emission intensity *versus* the Sm^{3+} content. (c) CIE chromaticity coordinates for these phosphors.

Table 4 CIE chromaticity coordinates for CLSO:9%Tb^{3+}, *y*%Sm^{3+} Phosphors

Sample no.	Sample	CIE coordinates (*x*, *y*)
1	CLSO:9%Tb^{3+}, 1%Sm^{3+}	(0.403, 0.476)
2	CLSO:9%Tb^{3+}, 5%Sm^{3+}	(0.420, 0.454)
3	CLSO:9%Tb^{3+}, 7%Sm^{3+}	(0.435, 0.435)
4	CLSO:9%Tb^{3+}, 9%Sm^{3+}	(0.422, 0.421)
5	CLSO:9%Tb^{3+}, 11%Sm^{3+}	(0.402, 0.398)
6	CLSO:9%Tb^{3+}, 13%Sm^{3+}	(0.393, 0.387)

Table 5 CIE chromaticity coordinates for CLSO:3%Ce^{3+}, 9%Tb^{3+}, *y*%Sm^{3+} phosphors

Sample no.	Sample	CIE coordinates (*x*, *y*)
1	CLSO:3%Ce^{3+}, 9%Tb^{3+}, 1%Sm^{3+}	(0.240, 0.270)
2	CLSO:3%Ce^{3+}, 9%Tb^{3+}, 5%Sm^{3+}	(0.268, 0.272)
3	CLSO:3%Ce^{3+}, 9%Tb^{3+}, 7%Sm^{3+}	(0.295, 0.285)
4	CLSO:3%Ce^{3+}, 9%Tb^{3+}, 9%Sm^{3+}	(0.284, 0.280)
5	CLSO:3%Ce^{3+}, 9%Tb^{3+}, 11%Sm^{3+}	(0.277, 0.276)

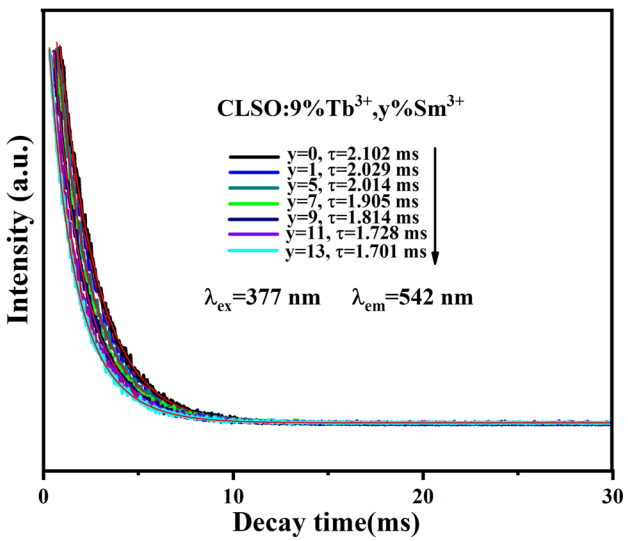

Fig. 9 Decay curves for Tb^{3+} emission from CLSO:9%Tb^{3+}, *y*%Sm^{3+} (*y* = 0–13) (excited at 377 nm, monitored at 542 nm).

of eqn (5), showing a decrease when more Sm^{3+} ions were imported as 0%, 1%, 5%, 7%, 9%, 11% and 13% mol concentrations, which strongly indicated that Tb^{3+} could effectively transfer energy to Sm^{3+}. The ET efficiencies of $Tb^{3+} \rightarrow Sm^{3+}$ were also resolved using eqn (6), as shown in the trend curve of Fig. 10, from which one can note the continuous growth of η_T with the Sm^{3+} concentrations rising, with the greatest value of 90% obtained at $y = 13$.

3.5 Energy-transfer mechanism and white light emission for CLSO:Ce^{3+}, Tb^{3+}, Sm^{3+}

The white light emission for the energy-transfer system with the tri-doped single substrate can drive innovation for high-quality w-LEDs. As contrasted in Fig. 11a, the excitation spectrum for CLSO:3%Ce^{3+}, 9%Tb^{3+}, 7%Sm^{3+} with the emission of Sm^{3+} monitored at 598 nm mainly comprised the absorption bands of Ce^{3+}, Tb^{3+} and Sm^{3+} ions. Meanwhile, under particular excitation (347 nm), the three characteristic emission bands of Ce^{3+},

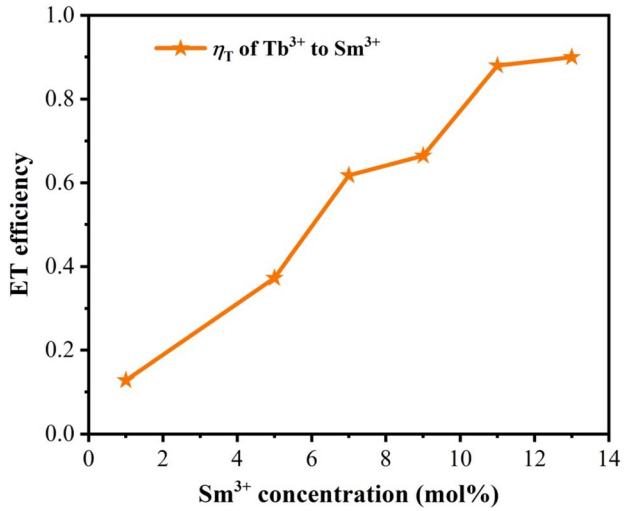

Fig. 10 Dependence of the energy-transfer efficiency η_T on Sm^{3+} concentration.

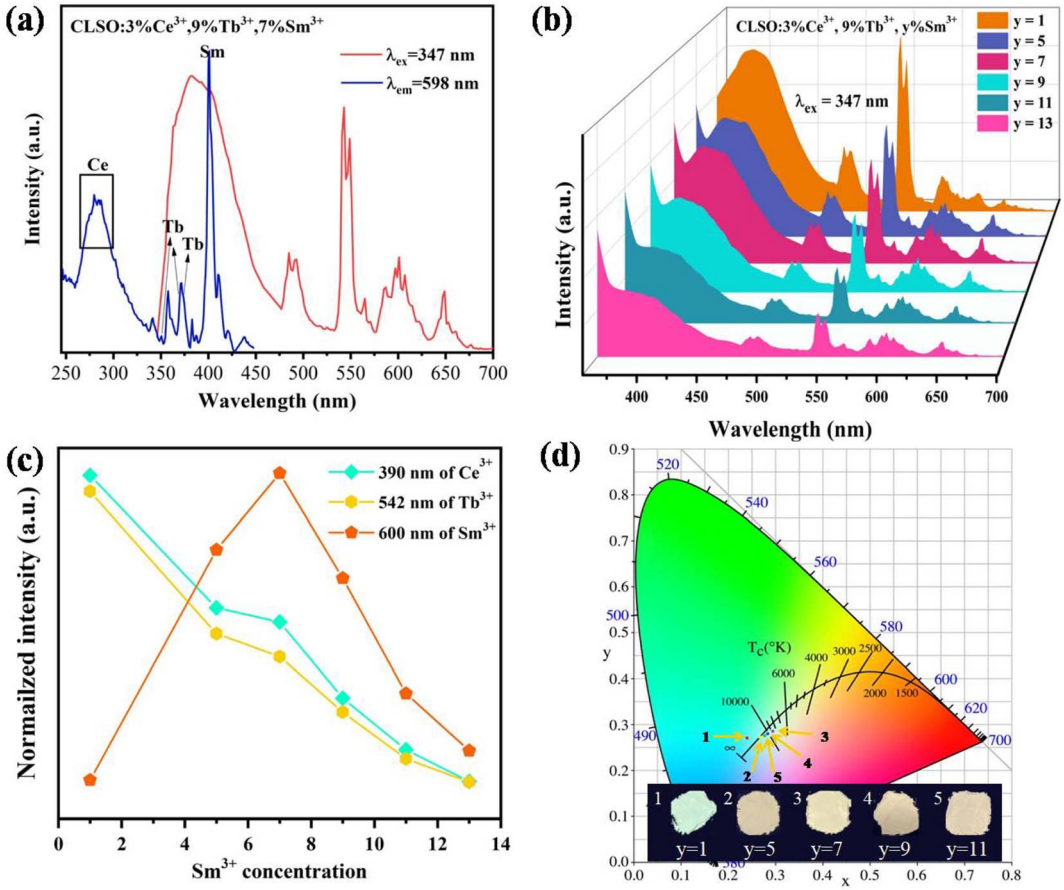

Fig. 11 (a) PLE spectrum and PL spectrum for CLSO:3%Ce^{3+}, 9%Tb^{3+}, 7%Sm^{3+} samples. (b) PL spectra of CLSO:3%Ce^{3+}, 9%Tb^{3+}, y%Sm^{3+} (y = 1–13) samples. (c) Changes in the intensity as a function of the Sm^{3+} concentration. (d) CIE chromaticity coordinates for the corresponding phosphors.

Tb^{3+} and Sm^{3+} were produced simultaneously. Accordingly, the emission spectra with fixing the contents of Ce^{3+} and Tb^{3+} at 3% and 9%, and varying the Sm^{3+} concentration were obtained, as shown in Fig. 11b. Meanwhile Fig. 11c presents the curve graphs for the change in the intensity as a function of the Sm^{3+} concentration. With an increase in Sm^{3+} ions, Ce^{3+}/Tb^{3+} emission was weakened, while Sm^{3+} emission was elevated until y = 7, which was a consequence of energy transfer for the Ce^{3+} → Tb^{3+} → Sm^{3+} tri-doped system. The process causes the CLSO:3%Ce^{3+}, 9%Tb^{3+}, y%Sm^{3+} system to vary in the blue to white zones with varying the Sm^{3+} ion concentration, with white light emission arising at y = 7 and 9, while the relevant coordinate were (0.295, 0.285) and (0.284, 0.280), respectively, as shown in Fig. 11d and Table 5.

The lifetime curves of Ce^{3+} in CLSO:3%Ce^{3+}, 9%Tb^{3+}, y%Sm^{3+} were also assessed to validate the energy transfer for Ce^{3+} → Tb^{3+} → Sm^{3+}(Fig. 12), and the decay curve for the Ce^{3+}, Tb^{3+} co-doped CLSO could be well fitted with a double-exponential function, eqn (4), while that of the other tri-doped samples could be well-explained by a triple-exponential equation as follows:

$$I = I_0 + A_1 \exp(-t/\tau_1) + A_2 \exp(-t/\tau_2) + A_3 \exp(-t/\tau_3) \quad (7)$$

In a previous study, the existence of three luminescence centers and their energy transfer were preliminarily proved by the excitation spectrum of a CLSO:3%Ce^{3+}, 9%Tb^{3+}, 7%Sm^{3+} sample (Fig. 11a) and emission spectra of CLSO:3%Ce^{3+}, 9%

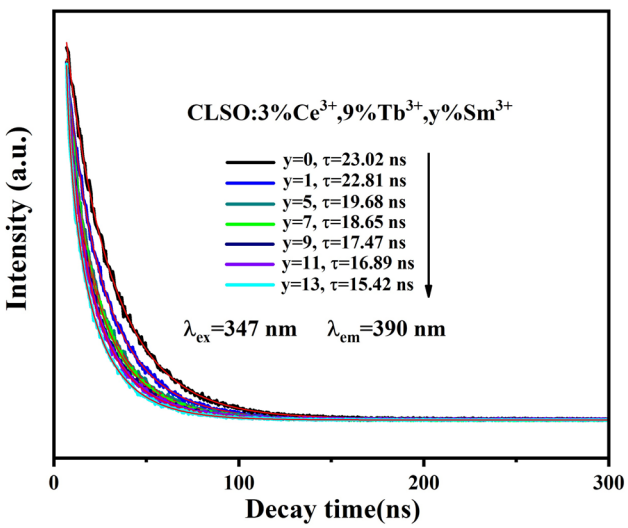

Fig. 12 Decay curves for Ce^{3+} emission from CLSO:3%Ce^{3+}, 9%Tb^{3+}, y%Sm^{3+} (y = 0–13) (excited at 347 nm, monitored at 390 nm).

Tb^{3+}, y%Sm^{3+} (y = 1–13) samples (Fig. 11b). Therefore, the decay curves (value) for CLSO:3%Ce^{3+}, 9%Tb^{3+}, y%Sm^{3+} (y = 1–13) should be made up of three parts: the emission from Ce^{3+} ions (luminescence center 1), the effect from Tb^{3+} ion emission (luminescence center 2) and the effect from Sm^{3+} ion emission (luminescence center 3), and the three luminescence centers work together (the energy transfer effect) to determine the final decay curves (value). Hence, the decay curve for the tri-doped samples could be well-explained by a triple-exponential equation, indicating that the decay curves can be determined and influenced by the three luminescence centers. The τ values were determined to be 23.02, 22.81, 19.68, 18.65, 17.47, 16.89 and 15.42 ns, respectively (with y = 0, 1, 5, 7, 9, 11, 13 for the Sm^{3+} content). The increasing of attenuation for Ce^{3+} with more Sm^{3+} ions launching is the embodiment of energy transfer for tri-doped system.

A schematic model of the energy level is exhibited in Fig. 13 and briefly shows the photoelectron transitions and energy transfer in the Ce^{3+}, Tb^{3+} and Sm^{3+} tri-doped CLSO. Upon 347 nm excitation, the ground state electrons in Ce^{3+} ions were excited to the excited state (5d) and subsequently attenuated to the lowest excited band. Then a portion of the excited electrons fall back to the 4f ground level for $^2F_{5/2}$ and $^2F_{7/2}$, producing the bandwidth blue-violet emission of Ce^{3+} ions. The energy transfer for $Ce^{3+} \rightarrow Tb^{3+} \rightarrow Sm^{3+}$ in the tri-doped system is the result of the following three processes: (1) While the other portion of the excited electrons for Ce^{3+} ions might transfer energy to Tb^{3+} firstly, this happens due to the overlapping of Ce^{3+} emission spectrum and Tb^{3+} excitation spectrum ($Ce^{3+} \rightarrow Tb^{3+}$), and then from the $^5D_4$ state for Tb^{3+} ions eventually to Sm^{3+} corresponding to the ignorable energy discrepancy between Tb^{3+} and Sm^{3+}, wherein Tb^{3+} ions having the function of transmission intermediary. This can be expressed as $Ce^{3+} \rightarrow Tb^{3+} \rightarrow Sm^{3+}$. (2) Moreover, Tb^{3+} can also transfer self-absorbed energy to Sm^{3+} (the energy Tb^{3+} absorbs from ultraviolet light), expressed as $Tb^{3+} \rightarrow Sm^{3+}$. (3) The process where Ce^{3+} directly transfers energy to Sm^{3+} and not *via* Tb^{3+} is non-negligible, and happens due to the overlapping of the Ce^{3+} emission spectrum and Sm^{3+} excitation spectrum, expressed as $Ce^{3+} \rightarrow Sm^{3+}$. The Sm^{3+} emission intensity heightening and that of Ce^{3+}, Tb^{3+} being in the opposite direction are the effects of the combined actions in the three-step energy transfer approach. Ultimately, white light emission is realized based on the strength of the energy transfer for $Ce^{3+} \rightarrow Tb^{3+} \rightarrow Sm^{3+}$ in the tri-doped system.

3.6 Performance of LED prototypes

Abundant research work should be devoted to the thermal quenching effect of phosphors, since LED devices usually operate at higher temperature. As shown in Fig. 14, the emission spectra in the case of variable temperature for CLSO:3% Ce^{3+}, 9%Tb^{3+}, y%Sm^{3+} (y = 7, 9) phosphors were measured. A similar thermal stability was embodied in the emission intensities of the two samples with the temperature increasing. The phosphor CLSO:3%Ce^{3+}, 9%Tb^{3+}, 9%Sm^{3+} displayed no significant differences in the blue, green and red characteristic emission bands with increasing the temperature from 298 to 473 K. While the relative intensity for Ce^{3+} ions still maintained 75% of the initial value recorded at 473 K, in contrast Tb^{3+} and Sm^{3+} emission declined slightly more, but still preserved 65% and 60% of their initial values. Overall, the intensity of CLSO:3%Ce^{3+}, 9%Tb^{3+}, y%Sm^{3+} (y = 7, 9) phosphors decreased to a slight degree with the temperature rising. The Arrhenius equation can be employed to determine the activation energy barrier (ΔE) for further explaining the thermal quenching process:[40]

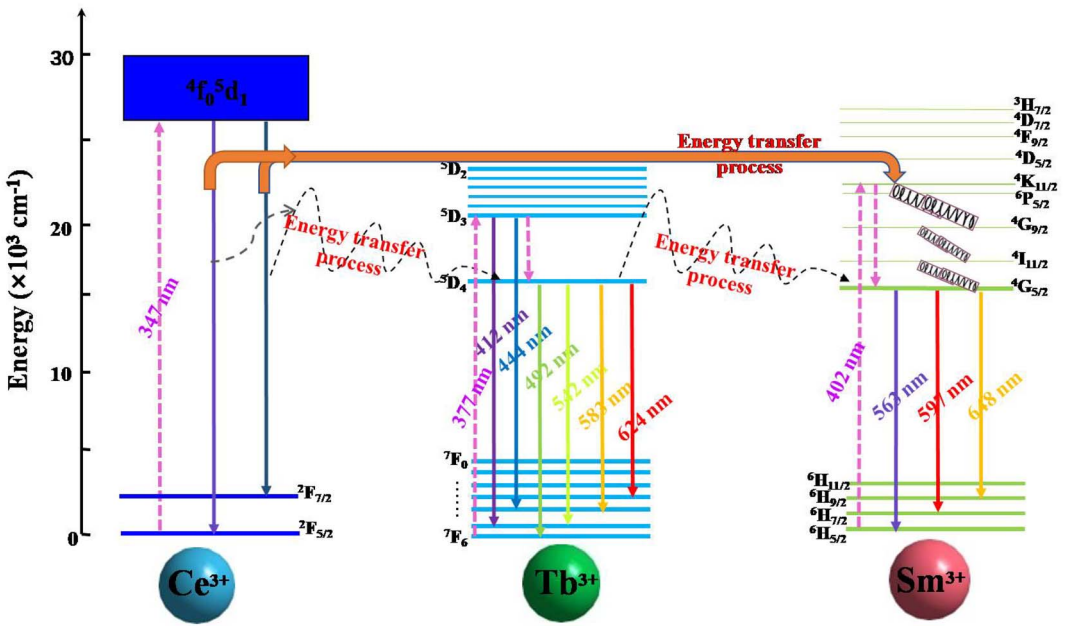

Fig. 13 Proposed energy-level mechanism diagram for energy transfer for $Ce^{3+} \rightarrow Tb^{3+} \rightarrow Sm^{3+}$ in the CLSO tri-doped system.

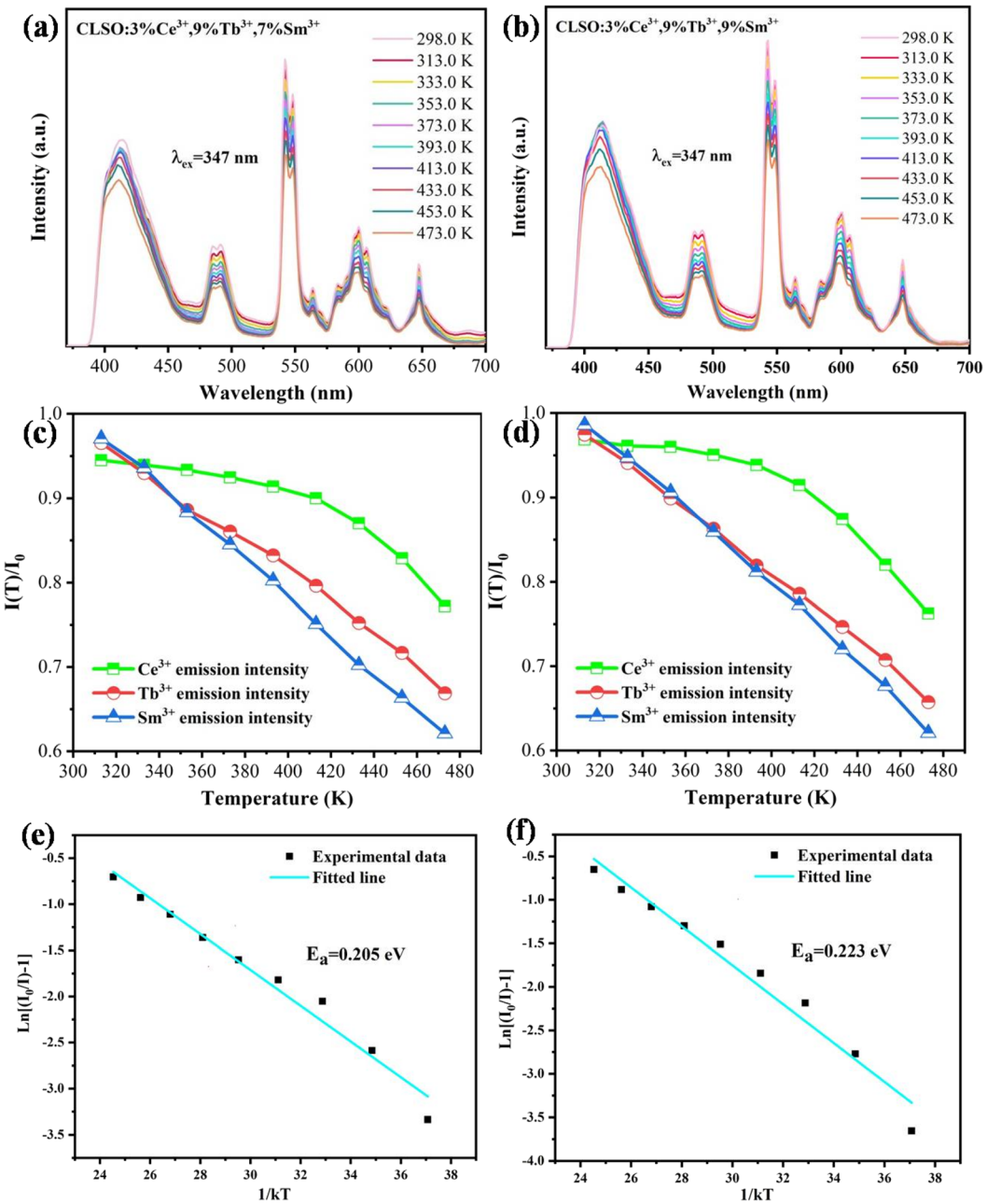

Fig. 14 Temperature-dependent emission spectra for (a) CLSO:3%Ce^{3+}, 9%Tb^{3+}, 7%Sm^{3+} and (b) CLSO:3%Ce^{3+}, 9%Tb^{3+}, 9%Sm^{3+} phosphors excited at 347 nm. Temperature-dependent normalized PL intensities of Ce^{3+}, Tb^{3+} and Sm^{3+} in (c) CLSO:3%Ce^{3+}, 9%Tb^{3+}, 7%Sm^{3+} and (d) CLSO:3%Ce^{3+}, 9%Tb^{3+}, 9%Sm^{3+}. $\ln[(I_0/I) - 1]$ *versus* $1/kT$ plot and the activation energy of (e) CLSO:3%Ce^{3+}, 9%Tb^{3+}, 7%Sm^{3+} and (f) CLSO:3% Ce^{3+}, 9%Tb^{3+}, 9%Sm^{3+} phosphors.

$$\frac{I}{I_0} = \left[1 + C\exp\left(-\frac{\Delta E}{kT}\right)\right]^{-1} \quad (8)$$

where, I_0 is the initial intensity; I is the emission intensity at a certain temperature, C is a constant and k is Boltzmann's constant. The linear fitting of $\ln[(I_0/I) - 1]$ and $1/kT$ in Fig. 14e and f manifested that the activation energy for CLSO:3%Ce^{3+}, 9%Tb^{3+}, y%Sm^{3+} (y = 7, 9) was 0.205 eV and 0.223 eV, respectively. In recent years, some excellent phosphors have been reported, such as $Ca_2YZr_2(AlO_4)_3$:Ce^{3+}, Tb^{3+},[41] $Tb_3Al_5O_{12}$:Ce^{3+}, Mn^{2+},[20] K_2NbF_7:Mn^{4+},[42] their emission intensity has declined to below 60% of the initial value at 393 K. Therefore, compared with these representative phosphors, it was shown that the CLSO:3%Ce^{3+}, 9%Tb^{3+}, y%Sm^{3+} (y = 7, 9) phosphors had excellent thermal stability.

We attempted to manufacture prototypes of white LED single beads by coating CLSO:3%Ce^{3+}, 9%Tb^{3+}, y%Sm^{3+} (y = 7, 9) phosphors on commercial 360 nm UV chips, which gives impetus to the practical application of phosphors. The electroluminescence spectra and physical photographs for two LED

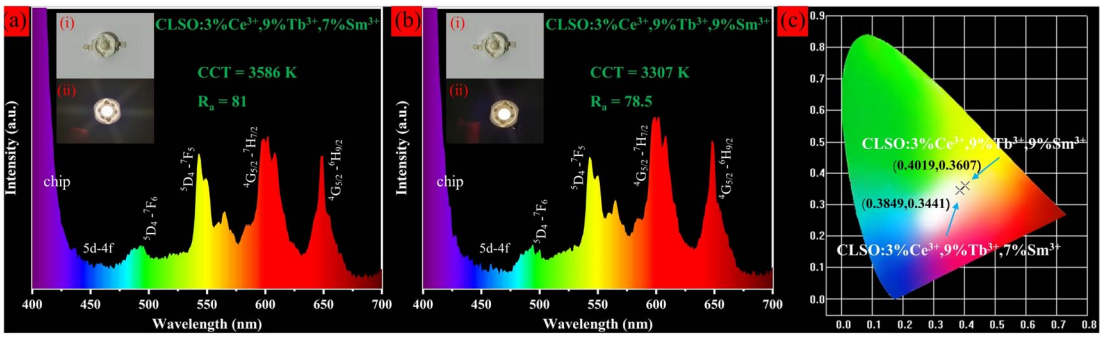

Fig. 15 Electroluminescence spectra and photographs of white LED prototypes fabricated by combining a 360 nm UV chip with (a) CLSO:3% Ce^{3+}, 9%Tb^{3+}, 7%Sm^{3+} and (b) CLSO:3%Ce^{3+}, 9%Tb^{3+}, 9%Sm^{3+} phosphors. (c) CIE chromaticity coordinates for corresponding WLED devices.

devices at 20 mA forward bias current are shown in Fig. 15. It was apparent that the spectra had no disparity compared with the emission spectra of phosphors, comprising a blue-green-red emission band within the coverage for the entire visible region, which originated from the emission of Ce^{3+}, Tb^{3+} and Sm^{3+} ions in CLSO:3%Ce^{3+}, 9%Tb^{3+}, y%Sm^{3+} (y = 7, 9), respectively. The as-fabricated LED lamps emitted bright white light and the corresponding test parameters are shown in the illustration. The findings reveal that the two fabricated LED devices had chromaticity coordinates for the white light region, and the CCT and CRI were 3586 K, 81.0 (a), 3307 K, 78.5 (b), that is, normal white light and warm white light, respectively.[43,44] In relative terms, the white LED (a) was the more ideal one. Compared with current commercial white LEDs (YAG:Ce^{3+} + blue chip, CRI < 80, CCT ≈ 7750 K, a cool color white), a red component was added, and the CCT for 3586 K was advanced but slightly warmer (daily lighting white: 4000–5500 K), while the CRI for 81 is improved. These performances suggest that the CLSO:3%Ce^{3+}, 9%Tb^{3+}, y%Sm^{3+} (y = 7, 9) were favorable for providing high-quality white emission to apply in w-LEDs with UV chip excitation.

4. Conclusion

In this paper, single-phase $CaLa_4(SiO_4)_3O$:Ce^{3+}, Tb^{3+}, Sm^{3+} phosphors inducing white emission *via* the ET process for Ce^{3+} → Tb^{3+} → Sm^{3+} were successfully prepared. The Rietveld refinement demonstrated the dependability of the obtained crystal structure and the band gap energy was about 4.612 eV according to DFT calculations. Since Tb^{3+} ions were sensitized by Ce^{3+} ions and Sm^{3+} ions were sensitized by Ce^{3+} and Tb^{3+} ions, energy transfer could occur in the tri-doped system, and the ET processes for Ce^{3+} → Tb^{3+}, Tb^{3+} → Sm^{3+} and Ce^{3+} → Tb^{3+} → Sm^{3+} were explored in detail. The single-phase white emission was successfully promoted by means of the above ET process in the tri-doped system. Moreover, the emission intensity of CLSO:3%Ce^{3+}, 9%Tb^{3+}, y%Sm^{3+} (y = 7, 9) still maintained 75% of the initial value with the temperature rising from 298 to 473 K, indicating a prominent thermal quenching resistance. Finally, prototype WLED devices involving CLSO:3% Ce^{3+}, 9%Tb^{3+}, y%Sm^{3+} (y = 7, 9) phosphors were developed and tested, and the LED lamps displayed bright white light, with CCT = 3586 K, 3307 K and CRI = 81.0, 78.5, respectively. These results demonstrate the potential application value for the Ce^{3+}, Tb^{3+}, Sm^{3+} tri-doped single-phase phosphor in pc-WLEDs.

Conflicts of interest

There are no conflicts to declare.

Acknowledgements

This funding for the present work is supported by the Free Exploration Basic Research Project of Jilin Province Office of Science and Technology, China (YDZJ202201ZYTS649), the Major Project for the Field (2016009), Jilin Institute of Chemical Technology and Fundamental Research Cultivating Fund, Jilin Institute of Chemical Technology.

References

1 Z. Xia, Z. Xu, M. Chen and Q. Liu, *Dalton Trans.*, 2016, **45**, 11214–11232.
2 S. Gu, M. Xia, C. Zhou, Z. Kong, M. S. Molokeev, L. Liu, W.-Y. Wong and Z. Zhou, *Chem. Eng. J.*, 2020, **396**, 125208.
3 Y. Zhu, L. Fu, D. Wu, J. Peng, F. Du, X. Ye, L. Chen and W. Zhuang, *J. Lumin.*, 2021, **232**, 117854.
4 D. Wu, L. Fu, S. He, F. Xu, L. Liu, L. Yao, F. Du, J. Peng and X. Ye, *Ceram. Int.*, 2020, **46**, 25382–25391.
5 X. Huang, S. Han, W. Huang and X. Liu, *Chem. Soc. Rev.*, 2013, **42**, 173–201.
6 X. Zhang, L. Huang, F. Pan, M. Wu, J. Wang, Y. Chen and Q. Su, *ACS Appl. Mater. Interfaces*, 2014, **6**, 2709–2717.
7 P. Pust, P. J. Schmidt and W. Schnick, *Nat. Mater.*, 2015, **14**, 454–458.
8 S. Wu, P. Xiong, X. Liu, Y. Fu, Q. Liu, Y. Chao, Q. Dong, Y. Li, W. Chen, Y. Chen, Z. Ma and M. Peng, *J. Mater. Chem. C*, 2021, **9**, 3672–3681.
9 W. Yan, Y. Wei, M. S. Molokeev, S. Wang and G. Li, *J. Alloys Compd.*, 2022, **908**, 164621.
10 H. D. Nguyen, C. C. Lin and R. S. Liu, *Angew. Chem., Int. Ed.*, 2015, **54**, 10862–10866.
11 D. Liu, X. Yun, P. Dang, H. Lian, M. Shang, G. Li and J. Lin, *Chem. Mater.*, 2020, **32**, 3065–3077.
12 X. Yu, D. Yuan and X. Mi, *J. Alloys Compd.*, 2021, **857**, 157585.

13 G. Li, Z. Hou, C. Peng, W. Wang, Z. Cheng, C. Li, H. Lian and J. Lin, *Adv. Funct. Mater.*, 2010, **20**, 3446–3456.
14 X. Li, L. Zhou, J. Hong, S. He, X. Jing, M. D. Dramićanin, J. Shi and M. Wu, *J. Mater. Chem. C*, 2020, **8**, 6715–6723.
15 J. Long, F. Chu, Y. Wang, C. Zhao, W. Dong, X. Yuan, C. Ma, Z. Wen, R. Ma, M. Du and Y. Cao, *Inorg. Chem.*, 2017, **56**, 10381–10386.
16 J. Zhang and C. Jiang, *Mater. Res. Bull.*, 2014, **60**, 467–473.
17 Y. Kawano, S. W. Kim, T. Ishigaki, K. Uematsu, K. Toda, H. Takaba and M. Sato, *Opt. Mater. Express*, 2014, **4**, 1770–1774.
18 L.-F. Liu, G.-G. Wang, Q. Yang, B. Yan, H.-Y. Zhang and J.-C. Han, *Ceram. Int.*, 2018, **44**, 11693–11701.
19 C. Xu, Y. Song, H. Guan, Y. Sheng, P. Ma, X. Zhou, Z. Shi and H. Zou, *Phys. Chem. Chem. Phys.*, 2017, **19**, 22197–22209.
20 Y. Duan, C. Zhao, H. Lin, R. Hong, C. Tao, Z. Han, D. Zhang and S. Zhou, *Opt. Mater.*, 2021, **111**, 110670.
21 S. Shimono, T. Izaki, N. Tanaka, Y. Nanai, T. Morimoto, H. Kishimura and A. Aruga, *Mater. Res. Bull.*, 2021, **143**, 111441.
22 Y. Xiang, Z. Y. Liu, Y. Gao, L. Feng, T. Zhou, M. J. Liu, Y. Zhao and D. J. Gao, *Chem. Eng. J.*, 2023, **456**, 140901.
23 Y. Zhang, Y. Liang, S. Miao, D. Chen, S. Yan and J. Liu, *Inorg. Chem. Front.*, 2021, **8**, 5186–5194.
24 N. Liu, L. Mei, L. Liao, J. Fu and D. Yang, *Sci. Rep.*, 2019, **9**, 15509.
25 H. Liu, L. Liao, M. S. Molokeev, Q. Guo, Y. Zhang and L. Mei, *RSC Adv.*, 2016, **6**, 24577–24583.
26 K. Li, J. Fan, M. Shang, H. Lian and J. Lin, *J. Mater. Chem. C*, 2015, **3**, 9989–9998.
27 S. Unithrattil, H. J. Kim, K. H. Gil, N. H. Vu, V. H. Hoang, Y. H. Kim, P. Arunkumar and W. B. Im, *Inorg. Chem.*, 2017, **56**, 5696–5703.
28 X. Zhang, Q. Liu, J.-W. Luo, A. J. Freeman and A. Zunger, *Nat. Phys.*, 2014, **10**, 387–393.
29 X. Q. Wang, X. M. Han and C. M. Zhen, *J. Nanosci. Nanotechnol.*, 2011, **11**, 9714–9716.
30 X. Chen, Z. Xia and Q. Liu, *Dalton Trans.*, 2014, **43**, 13370–13376.
31 M. A. L. Marques, J. Vidal, M. J. T. Oliveira, L. Reining and S. Botti, *Phys. Rev. B: Condens. Matter Mater. Phys.*, 2011, **83**, 035119.
32 Z. Jiang, Y. Wang, Z. Ci and H. Jiao, *J. Electrochem. Soc.*, 2009, **156**, J317–J320.
33 M. Pepper, *Contemp. Phys.*, 1979, **20**, 483–485.
34 Z. G. Xia, C. G. Ma, M. S. Molokeev, Q. L. Liu, K. Ricket and K. R. Poeppelmeier, *J. Am. Chem. Soc.*, 2015, **137**, 12494–12497.
35 Y. Wang, J. Ding and Y. Wang, *J. Phys. Chem. C*, 2017, **121**, 27018–27028.
36 M. Zhao, H. Liao, L. Ning, Q. Zhang, Q. Liu and Z. Xia, *Adv. Mater.*, 2018, **30**, 1802489.
37 N. Zhang, J. Zheng, J. Gao, Y. Wu, R. Zhang, T. Li and C. Guo, *Dyes Pigm.*, 2017, **136**, 601–611.
38 D. Wu, Y. Xiao, L. Zhang, X. Dong, S. Zhao, W. Zhou, Q. Lu and J. Zhang, *J. Mater. Chem. C*, 2020, **8**, 17176–17184.
39 P. I. Paulose, G. Jose, V. Thomas, N. V. Unnikrishnan and M. K. R. Warrier, *J. Phys. Chem. Solids*, 2003, **64**, 841–846.
40 A. Zhang, M. Jia, Z. Sun, G. Liu, Z. Fu, T. Sheng, P. Li and F. Lin, *J. Alloys Compd.*, 2019, **782**, 203–208.
41 L. L. Sun, B. Devakumar, J. Liang, S. Y. Wang, Q. Sun and X. Y. Huang, *J. Mater. Chem. C*, 2019, **7**, 10471–10480.
42 J. Wu, Z. Y. Li, L. Luo, Y. H. Xiong, L. Y. Jiang, R. Guo and L. L. Meng, *J. Alloys Compd.*, 2021, **863**, 158058.
43 L. Zhou, P. Du, W. Li and L. Luo, *New J. Chem.*, 2019, **43**, 16445–16453.
44 X. Zhang, Z. An, R. Dong, Y. Song, K. Zheng, Y. Sheng, Z. Shi and H. Zou, *ACS Sustainable Chem. Eng.*, 2019, **7**, 10724–10733.